MDPI

Article

Polarization Splitter-Rotator Based on Multimode Waveguide Grating

Yannong Luo [1], Renyou Ge [2], Haozhi Luo [2], Meiyan Wu [3], Lidan Zhou [2], Makunda Aryal [4], Wenwei Li [1], Jianhui Yuan [3], Jian Xu [5], Quanxue Lan [6], Yongqing Li [4] and Xinlun Cai [2,*]

[1] Laboratory of Biomedical Photonics & Engineering, Life Science Institute, Guangxi Medical University, Nanning 530021, China; luoyannong@gxmu.edu.cn (Y.L.); liwenwei@gxmu.edu.cn (W.L.)
[2] State Key Laboratory of Optoelectronic Materials and Technologies, School of Electronics and Information Technology, Sun Yat-Sen University, Guangzhou 510275, China; gery@mail2.sysu.edu.cn (R.G.); luohzh3@mail2.sysu.edu.cn (H.L.); zhould@mail2.sysu.edu.cn (L.Z.)
[3] Laboratory of Biomedical Photonics & Engineering, School of Basic Medical Sciences, Guangxi Medical University, Nanning 530021, China; wumeiyan@stu.gxmu.edu.cn (M.W.); jianhui831110@gxmu.edu.cn (J.Y.)
[4] Department of Physics, East Carolina University, Greenville, NC 27858-4353, USA; aryalm18@students.ecu.edu (M.A.); liy@ecu.edu (Y.L.)
[5] School of Economics and Commerce, South China University of Technology, Guangzhou 510640, China; jianxu@scut.edu.cn
[6] Longgang Center for Disease Control and Prevention, Shenzhen 518172, China; lanquanxue@126.com
* Correspondence: caixlun5@mail.sysu.edu.cn

Academic Editors: John Rarity, Tullio Scopigno, Mike Taverne and Ying-Lung Daniel Ho

Publisher's Note: MDPI stays neutral with regard to jurisdictional claims in published maps and institutional affiliations.

Abstract: We demonstrate a polarization splitter rotator (PSR) based on multimode waveguide grating (MWG) on a silicon-on-insulator (SOI) platform. Bloch mode hybridization in mini-stopband is exploited to achieve high polarization conversion efficiency. The fabricated device yields a high extinction ratio of > 53 dB and > 31 dB, low crosstalk of < −26.4 dB and < −40 dB for the injected TE_0 and TM_0 mode, with average insertion loss of 1.2 dB and 1.5 dB in the wavelength regime 1552 nm–1562 nm. Such a device shows great design flexibility and an easy fabrication process, serving as a good candidate in integrated polarization diversity circuits, especially for applications requiring spectra manipulation. Additionally, the polarization conversion approach provides opportunities to develop novel polarization management devices.

Keywords: polarization splitter rotator; multimode waveguide grating; silicon photonics

1. Introduction

Silicon-on-insulator (SOI) has become one of the most promising platforms for photonic integration benefiting from its low cost, high-density integration, and compatibility with CMOS fabrication processes. However, the high index contrast introduces significant polarization dependence, which makes silicon photonic devices incompatible with fiber communication applications where the polarization state in optical fiber is typically random. One efficient solution to eliminate the polarization sensitivity is to use a polarization splitter-rotator (PSR) [1–5], in which the TE_0 mode and TM_0 mode can be separated into two individual waveguides. Meanwhile, one of the polarization states will be converted to the orthogonal one, normally chosen as TE_0 mode considering that most devices are optimized only for TE_0 polarization. Such a polarization handling device is also desired on other material platforms, and has been demonstrated on platforms including InP [6,7], SiN [8] and lithium-niobate-on-insulator (LNOI) [9,10]. Vertical asymmetrical structures are normally required to implement polarization conversion schemes including covering different cladding material [1], fabricating a bi-level taper [11,12], or introducing additional top structures such as gold [13] and SiN [14]. The operation principle of PSRs can be classified into two categories of mode coupling [15] and mode evolution [16,17], according to the energy exchange path when polarization rotation. For mode coupling based PSRs,

phase-matching condition should be satisfied. The typical structures adopted are asymmetrical directional coupler (ADC) [18], tapered DC [19], bend DC [20,21], and so on. For mode evolution ones, mode hybridization between TM_0 mode and forward TE_1 mode can occur when light propagates along the adiabatic taper or multimode waveguide [22]. It should be noted that all the reported PSRs are designed for broadband operation, aiming as universal schemes for realizing polarization-transparent photonic integrated circuits (PICs). However, for some critical applications such as polarization insensitive wavelength division (de)multiplexer [23,24], wavelength selective devices such as arrayed waveguide gratings (AWGs) are subsequently required to implement wavelength multiplexing [25], inevitably incurring extra insertion loss and footprint and design complexity to the whole on-chip system. Exploiting novel polarization conversion mechanisms and developing new functional devices are desirable for PICs application.

Mini-stopband (MSB) is derived from the anti-crossing between Bloch modes [26,27]. There have been numerous interesting applications based on MSB, mostly in two dimensional photonic crystal (2D-PhC) such as pulse compression [28], coarse wavelength selection [29], optical filters [30], and selective mirroring in PhC lasers [31,32]. Several functional components based on MSB have also been demonstrated including polarization beam splitter [33] and tunable optical band stop filters [34], in one dimensional photonic crystal (1D-PhC). However, the authors have never considered in particular the coupling between Bloch modes with different polarization, and resultant polarization conversion in multimode waveguide grating (MWG).

In this paper, we demonstrate a novel MWG-based PSR. An anti-crossing of Bloch modes in MSB is exploited to archive highly efficient polarization rotation. The proposed PSR boasts a high extinction ratio, low crosstalk, an easy fabrication process, and great design flexibility. Additionally, such a device can be further cascaded with grating assisted contra-directional couplers (contra-DCs) [35,36], paving the way for critical applications such as polarization insensitive wavelength division (de)multiplexer [23,24] and multi-channel polarization-multiplexed differential quadrature phase-shift keying (PM-DQPSK) transceiver [37,38].

2. Device Structure and Working Principle

The proposed PSR is schematically illustrated in Figure 1, and consists of a linearly tapered multimode waveguide grating (MWG) and adiabatic coupler (AC). The silicon strip waveguides are 220 nm high sitting on a 2 μm buried oxide layer with air cladding, for the demand of vertical symmetry breaking. For the injected TE_0 mode, the light beam keeps propagating along AC, MWG, and linearly tapered waveguide (length L_2), then exits at the through (TRU) port. In the case of TM_0 input, the mode is first preserved in the AC region (length L_1, Gap G), then reversely coupled to be the TE_1 mode by MWG due to the satisfied phase-matching condition and Bloch mode hybridization. In the AC section, the backward TE_1 mode finally evolves into a TE_0 mode of the isolated bottom taper waveguide (width from W_4 to W_3) and bends away to the cross (CRO) port.

The structure parameters of width, period, grating number, and corrugation width in the uniform MWG region are denoted by W_2, Λ, N, and δw, respectively, as labeled in Figure 1b. As a potential application scenario, we also propose an easy architecture of a polarization insensitive wavelength duplexer, simply by cascading MWG-based PSR and grating assisted contra-directional coupler. As depicted in Figure 1c, the injected TM_0 mode will be backward converted to TE_0 by PSR and dropped at different ports because of the different grating period Λ. Meanwhile, the injected TE_0 mode propagates through the whole PSRs region, is then dropped to different ports by contra-DCs. Note that the longitudinal-apodization design is normally requires suppressing the sidelobe of the spectra and reducing channel crosstalk.
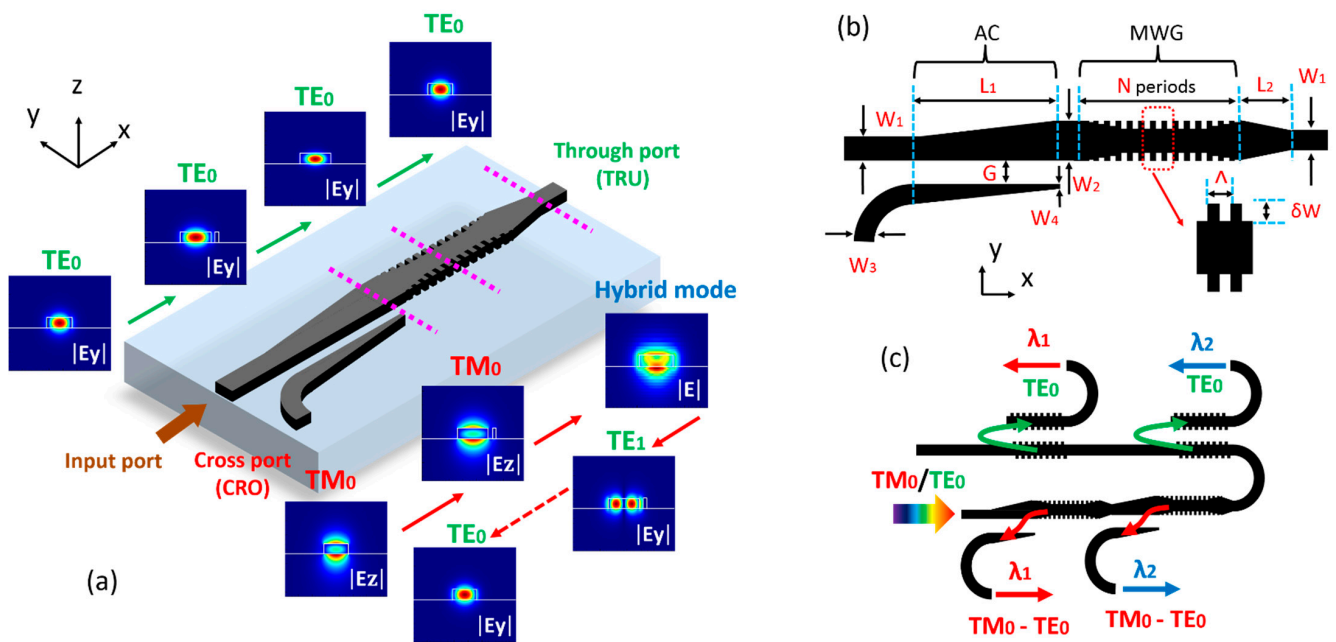
Figure 1. Schematic configuration of the proposed PSR. (**a**) Three-dimensional structure and (**b**) top view of the device. (**c**) Architecture of polarization insensitive wavelength duplexer based on MWG-based PSRs and contra-DCs.

To illustrate the working principle of the proposed PSR, we calculated the photonic band structure of uniform MWG using the three-dimensional finite-difference time-domain (3D-FDTD) method, with structure parameters: Λ = 414 nm, W_2 = 900 nm, δw = 100 nm, fill factor ff = 0.5. For the unit cell, non-uniform meshing is utilized with minimum mesh sizes $\Delta x_{min} = \Delta y_{min}$ = 10 nm, and Δz_{min} = 20 nm. Bloch periodic boundary conditions are imposed on the two surfaces perpendicular to the *x*-axis, and perfectly matched layer (PML) boundary conditions are applied on the other surfaces. Figure 2a shows the band structure of TE_0, TE_1, and TM_0 Bloch mode. The photonic band gaps (PBGs) are located at 187.8 THz–190.2 THz, 200.07 THz–201.2 THz, respectively, which means that there is no allowed mode in uniform MWG. Anti-crossing between TM_0 and TE_1 modes can also be observed, giving rise to a MSB at frequencies ranging from 194.0 THz to 195.3 THz (or wavelengths from 1.536 µm to 1.547 µm). Hence, the input TM_0 mode located in MSB can be converted to backward TE_1 Bloch mode, and vice-versa. Note that the conversion between the TM_0 and TE_1 Bloch modes in the uniform MWG should satisfy the phase matching condition: $\lambda_c/\Lambda = (Neff_1 + Neff_2)$, where $Neff_1$ and $Neff_2$ represent the effective refractive indices of the two coupled Bloch modes, and λ_c is central wavelength. The group indices Ng_{TE1} and Ng_{TM0} of both modes can be extracted from the slope of their dispersion relation, taken far from the coupling region [27]. The value of coupling coefficient κ can be derived by the following expression [39]:

$$\kappa = \pi N_g \Delta\lambda / \lambda_c^2 \tag{1}$$

where $\Delta\lambda$ is bandwidth of MSB, and $N_g = \left(N_{gTE0} + N_{gTM1}\right)/2$. For the uniform MWG considered above, the parameters extracted from the dispersion diagram of Figure 2a are Ng_{TE1} = 5.05, Ng_{TM0} = 4.11, and $\Delta\lambda/\lambda_c^2 = 0.463 \times 10^3$ m^{-1}, leading to $\kappa = 6.66 \times 10^3$ m^{-1}. This value is lower than the one of common waveguide Bragg gratings without polarization conversion, typically > 50×10^3 m^{-1} [40]. Additionally, we can effectively tune κ by using lateral phase delay modulation [41], for the purpose of apodization design. Figure 2b shows the local picture of MSB associated to the coupling between TM_0 and TE_1 Bloch modes. The electric field patterns are represented in Figure 2c,d.
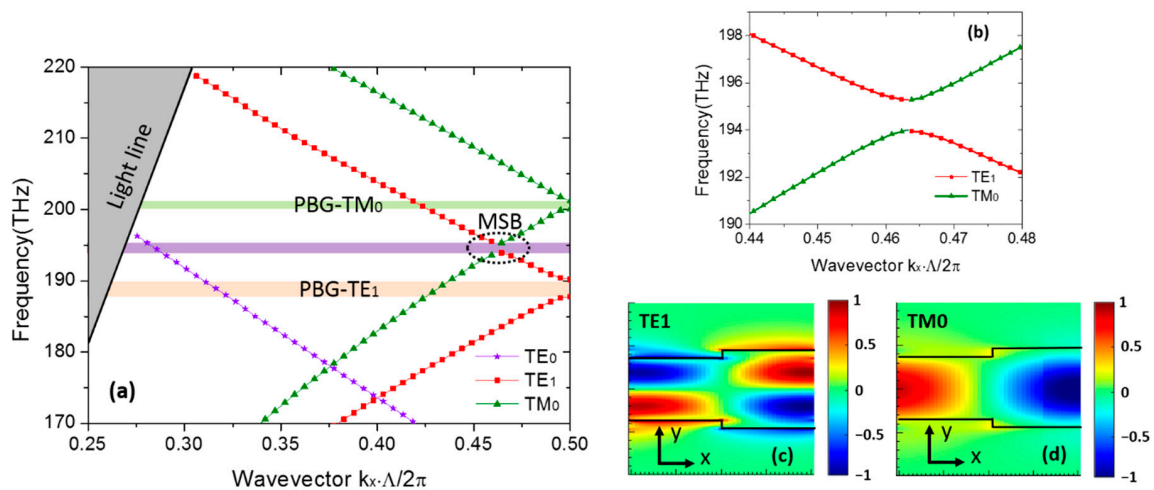
Figure 2. (**a**) Photonic band structure of uniform MWG. (**b**) Local picture of MSB associated to the coupling of TM_0 mode and TE_1 mode. Electric field patterns associated to (**c**) TE_1 mode (y-component, E_y) and (**d**) TM_0 mode (z-component, E_z).

Figure 3a shows the transmission and reflection spectra of uniform MWG with N = 100 when TE_0 and TM_0 mode are injected. The results are calculated using uniform meshing with $\Delta x_{min} = \Delta y_{min} = \Delta z_{min}$ = 20 nm, which ensure accuracy and calculation efficiency. One MSB ranging from 1.541 μm to 1.551 μm is observed; the reflection of the TM_0 mode is about 96%. We note that the transmission of input TE_0 mode is near 96% in MSB, while the major component of backward fields is TM_1 mode. However, this crosstalk is negligible due to the weak reflection and large propagation loss of TM_1 mode for the proposed device.
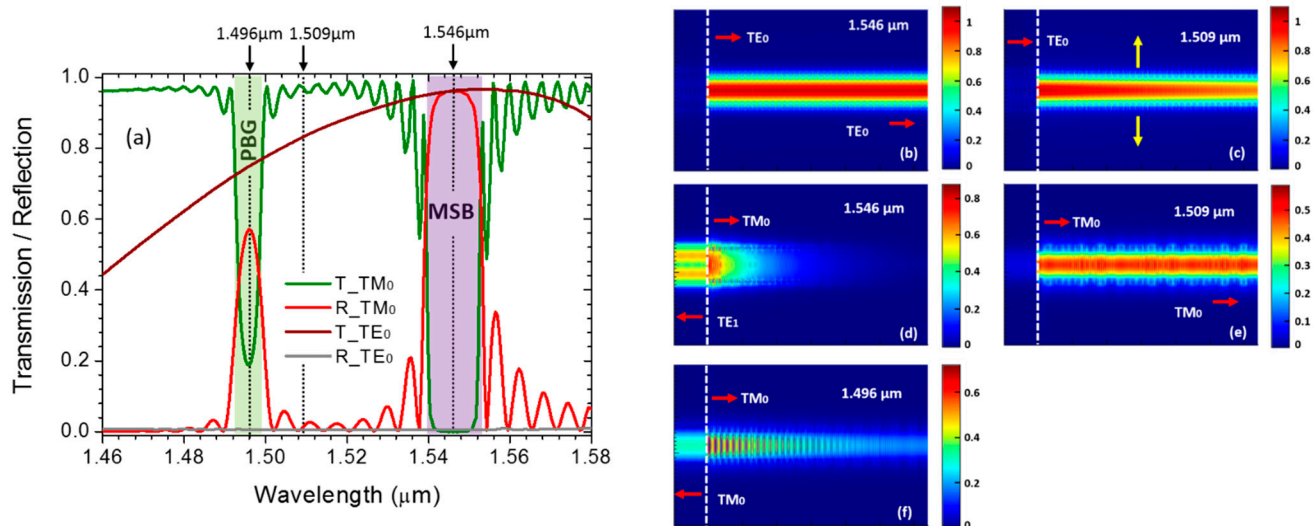

Figure 3. (**a**) Transmission and reflection spectra of uniform MWG. The light propagation profiles (electric field intensity |E|) in uniform MWG section when TE_0 mode and TM_0 mode are injected, at wavelengths of (**b**,**d**) 1.546 μm, (**c**,**e**) 1.509 μm, and (**f**) 1.496 μm.

We further simulate light propagation profiles in uniform MWG using 3D-FDTD, at typical wavelengths of 1.546 μm, 1.509 μm, and 1.496 μm, which are presented in Figure 3b–f. As predicted in the band structure, the launched TE_0 mode can maintain its polarization and propagate through uniform MWG (Figure 3b), at a wavelength of 1.546 μm. Meanwhile, the TE_0 mode will be gradually attenuated as a radiation mode being located above the light line (Figure 3c), at a wavelength of 1.509 μm (198.8 THz), with a transmission of 83%. For the launched TM_0 mode at 1.546 μm, the major component of backward field is TE_1 mode, as shown in Figure 3d. TM_0 mode is gradually attenuated

at a wavelength of 1.496 μm due to being located in the PBG (Figure 3f), while freely propagating at a wavelength of 1.509 μm as a purely Bragg-guided mode (Figure 3e).

To reduce insertion loss and suppress back-reflection incurred by mode mismatch between strip waveguide and uniform MWG, two linearly tapered gratings are utilized at both ends of the uniform MWG with minimum sidewall corrugation δw_{min}, minimum period Λ_{min}, and grating number N', as seen in Figure 4a. The $TM_0 - TE_1$ conversion efficiency is equal to the fraction of power reflected into TE_1 mode, which can be extracted utilizing the Mode Expansion Monitor. The transmission and reflection as a function of Λ_{min} are shown in Figure 4b. We can see that there is a linear variation region (340 nm < Λ_{min} < 390 nm) for TE_0 mode, and a local minimum reflection of −46 dB for TM_0 mode when Λ_{min} = 380 nm, which corresponds to the highest $TM_0 - TE_1$ conversion efficiency. This means that we need to make a trade-off between the transmission of TE_0 mode and the reflection of TM_0 mode. Here, the optimal Λ_{min} is determined to be 380 nm, which guarantees an acceptable transmission of 94.2% for TE_0 mode and the lowest reflection of TM_0 mode, and the highest conversion efficiency of $TM_0 - TE_1$. In the following simulation, linearly tapered gratings with δw_{min} = 10 nm, Λ_{min} = 380 nm and N' = 20 are adopted.

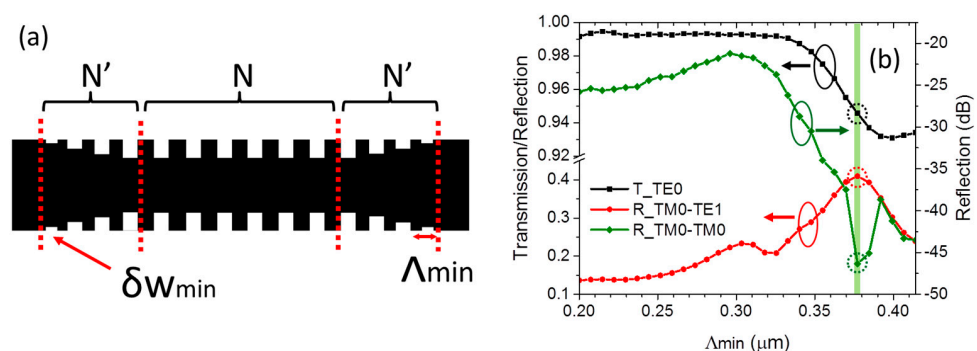**Figure 4.** (**a**) The schematic of linearly tapered MWG. (**b**) The transmission and reflection of linearly tapered MWG as a function of Λ_{min}, at 1.546 μm. Calculation using the following parameters: Λ = 414 nm, W_2 = 900 nm, δW = 100 nm, ff = 0.5, N = 10 for the uniform MWG and δw_{min} = 10 nm, N' = 20 for the taper section.

We investigate the influence of grating number N on spectra, keeping Λ = 0.414 μm, W_2 = 0.9 μm, δw = 0.1 μm, and ff = 50%, as shown in Figure 5a. It is seen that as N increases, the stopband edge becomes much steeper, and the maximum reflection increases significantly. Figure 5b presents the conversion efficiency and transmission as a function of grating number. As seen, the transmission of TE_0 mode is higher than 92% (−0.36 dB) when N = 200, and the conversion efficiency of $TM_0 - TE_1$ is improved by up to 98% (−0.22 dB). The transmission of TM_0 mode is about −46.9 dB at 1.546 μm, which could be even lower by increasing the grating number.
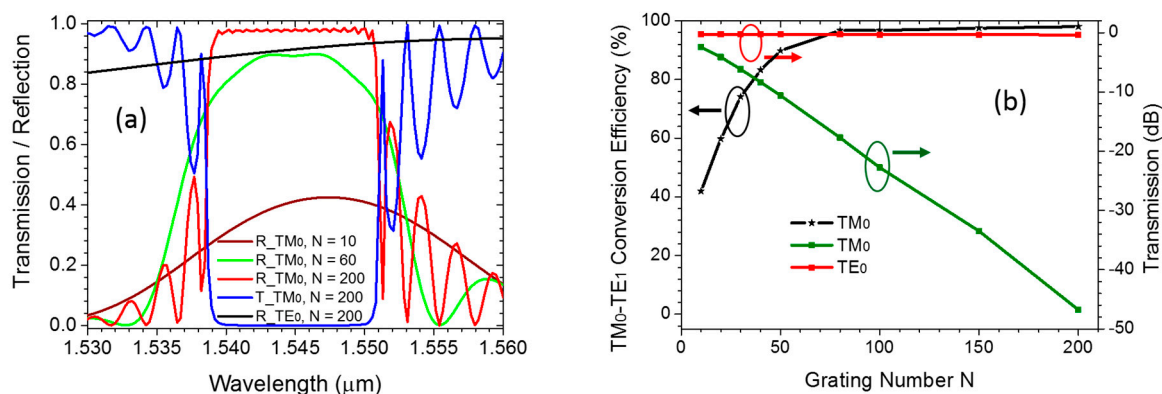

Figure 5. (**a**) The transmission and reflection spectra of linearly tapered MWG with different N. (**b**) TM_0-TE_1 conversion efficiency as a function of grating number N at 1.546 μm.

Next, we change the grating period Λ while keeping W_2 = 0.9 μm, δw = 0.1 μm and N = 200. The reflection spectra shown in Figure 6a indicates that stopband is red-shifted significantly as Λ increases. Slight ripple (lower than 1%) in stopband caused by mode mismatch is observed. Figure 6b presents the dependence of central wavelength λc and 1-dB bandwidth on grating period quantitatively. As seen, when Λ increases from 0.414 μm to 0.432 μm, λc increases linearly from 1.545 μm to 1.573 μm with slope $\frac{d\lambda c}{d\Lambda}$ = 1.5, and the bandwidth increases monotonously from 13 nm to 15 nm. Therefore, one can design operation wavelength of PSR by tuning grating period.
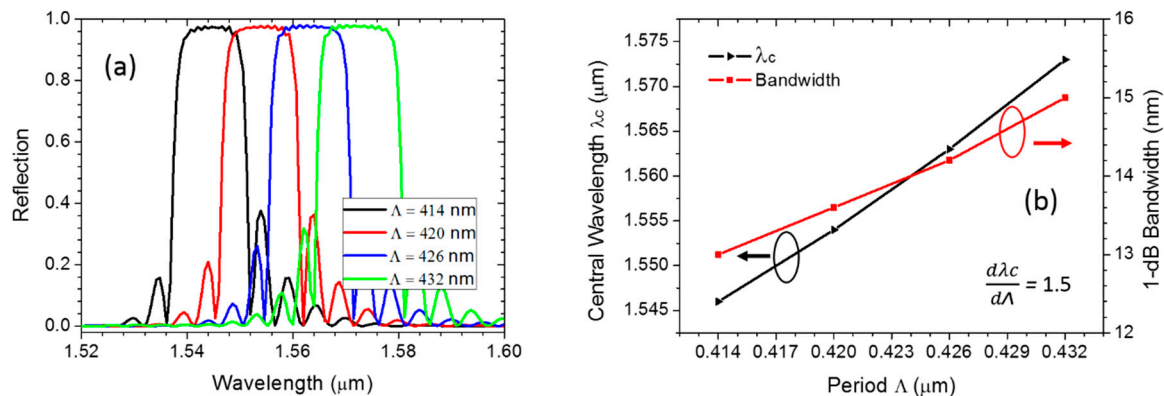

Figure 6. (**a**) The reflection spectra of linearly tapered MWG with different period Λ. (**b**) The central wavelength λc and bandwidth (90% CE) as a function of grating period Λ at wavelength of 1.546 μm.

The effect of corrugation width δw on reflection spectra is investigated when W_2 = 0.9 μm, Λ = 0.414 μm, and N = 200. As shown in Figure 7a, the stopband is red-shifted significantly as δw decreases, due to a variation of the effective refractive index in MWG. The reflection of central wavelength is diminished from 0.98 to 0.8 because of the decreasing grating strength. Figure 7b presents the dependence of central wavelength λc and 1-dB bandwidth of the stopband on the δw quantitatively. As seen, when δw increases from 50 nm to 112.5 nm, λc decreases with δw linearly from 1.578 μm to 1.535 μm with a slope $\frac{d\lambda c}{d\delta w}$ = −0.693, and the 1-dB bandwidth increases monotonously from 6 nm to 14 nm. This indicates that the MWG-based PSR is intrinsically characterized by a narrow operation bandwidth, due to the wavelength dependence of the grating.
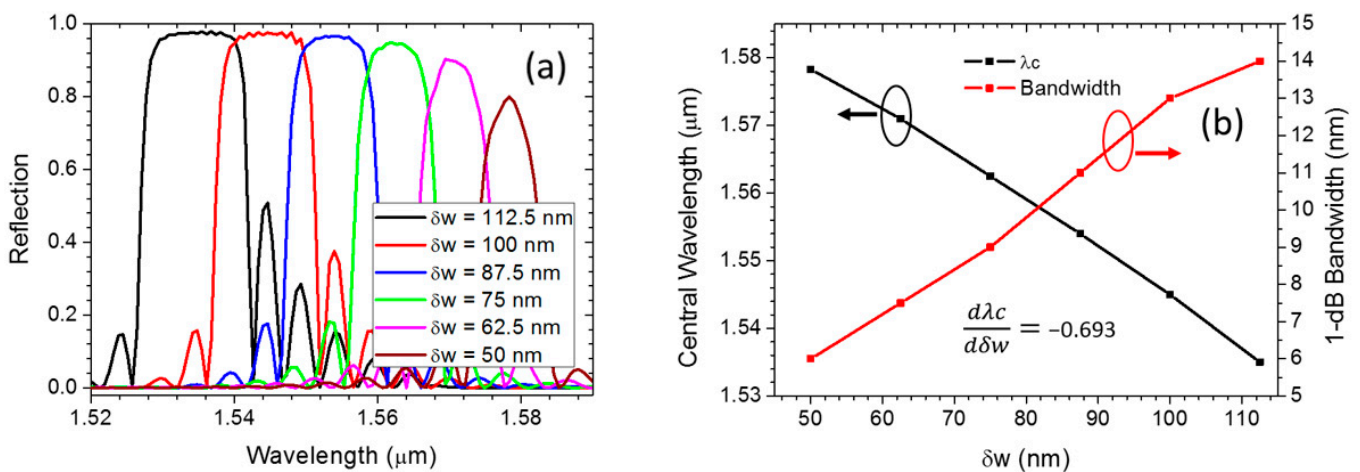

Figure 7. (**a**) The reflection spectra of linearly tapered MWG with different corrugation width δw. (**b**) The central wavelength and 1 dB bandwidth as a function of δw.

3. Device Performance and Analysis

An adiabatic coupler is adopted for the conversion between backward TE_1 mode and TE_0 mode because of its high conversion efficiency and large fabrication tolerance. The design parameters of AC and linear taper are optimized by the Eigenmode expansion (EME) method, which are listed as follows: $W_1 = 0.7$ μm, $W_2 = 0.9$ μm, $W_3 = 0.4$ μm, $W_4 = 0.1$ μm, $G = 0.12$ μm, $L_1 = 160$ μm, $L_2 = 3$ μm. The TE_1 to TE_0 conversion efficiency is up to 98.5% when $L_1 = 160$ μm at wavelength of 1.546 μm, as shown in Figure 8. Meanwhile, the mode conversion efficiency between the forward TM_0 mode and TE_1 mode decreases significantly, owing to the taper width (from W_1 to W_2), which is far away from the mode hybridization region, about 660 nm for the case of air cladding [22].
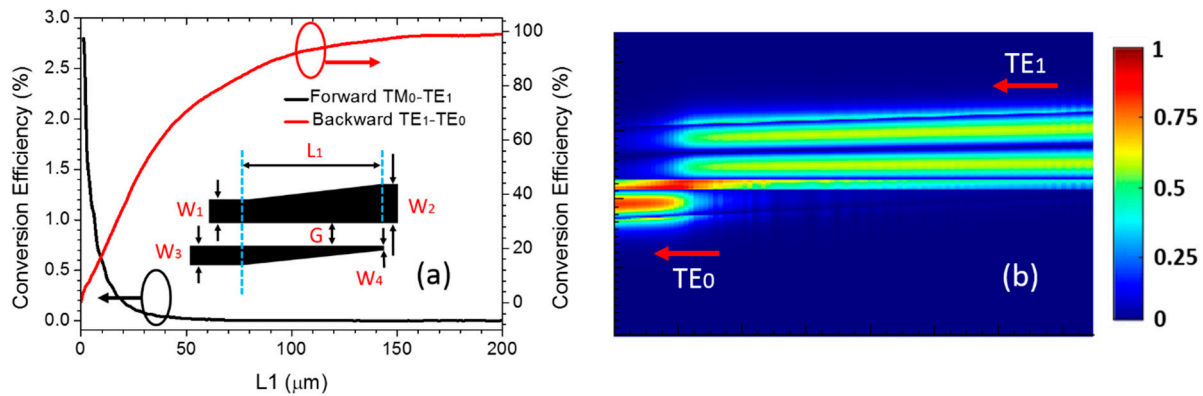

Figure 8. (**a**) The conversion efficiency of forward TM_0 –TE_1 and backward TE_1–TE_0, in AC section. (**b**) Simulated light propagation profiles (electric field intensity |E|) in adiabatic coupler when TE_1 mode propagates backward.

The light propagation profiles and transmission spectra of the whole PSR are simulated using structure parameters as following: $W_1 = 0.7$ μm, $W_2 = 0.9$ μm, $W_3 = 0.4$ μm, $W_4 = 0.1$ μm, $L_1 = 160$ μm, $L_2 = 3.0$ μm, $G = 0.12$ μm, $N = 200$, $\delta w = 0.1$ μm, $\Lambda = 0.414$ μm, $ff = 0.5$, $\delta w_{min} = 10$ nm, $\Lambda_{min} = 380$ nm and $N' = 20$. As shown in Figure 9a,b, the injected TE_0 mode propagates through the whole structure and outputs at the TRU port. Meanwhile, the injected TM_0 mode is first reversely converted to be TE_1 mode in the MWG section, then coupled to be TE_0 mode in the narrow waveguide of AC section, and finally output at the CRO port. The proposed PSR is evaluated by the performance metrics of insertion loss (IL), extinction ratio (ER), and crosstalk (CT), respectively [42]. The IL, ER, and CT for input TE_0 mode are defined as:

$$IL_{TE} = -10 \cdot \log_{10}\left(T_{TE}^{tru}\right) \tag{2}$$

$$ER_{TE} = -10 \cdot \log_{10}\left(T_{TM}^{tru}/T_{TE}^{tru}\right) \tag{3}$$

$$CT_{TE} = 10 \cdot \log_{10}\left(T_{TE}^{cro}/T_{TE}^{tru}\right) \tag{4}$$

The IL, ER and CT for input TM_0 mode are defined as:

$$IL_{TM} = -10 \cdot \log_{10}\left(T_{TE}^{cro}\right) \tag{5}$$

$$ER_{TM} = -10 \cdot \log_{10}\left(T_{TM}^{cro}/T_{TE}^{cro}\right) \tag{6}$$

$$CT_{TM} = 10 \cdot \log_{10}\left(T_{TE}^{tru}/T_{TE}^{cro}\right) \tag{7}$$

where T_{mode}^{port} means the transmission of mode at TRU port or CRO port. The calculated transmission spectra are shown in Figure 9c,d; we note that the IL_{TE} and IL_{TM} are both less than 0.5 dB over 10 nm bandwidth (1.54 μm–1.55 μm). The ER_{TE} is > 50 dB and CT_{TE} is < −39 dB for the TE_0 mode in the wavelength range of 1.53 μm–1.56 μm. Note that CT_{TE} is theoretically originated from the backward TM_1 mode excited by MWG. However, this impact is negligible for a fabricated device considering the large propagation loss of TM_1

mode, which is further confirmed by our experimental results. For the input TM_0 mode, ER_{TM} of > 30 dB and CT_{TM} of −48 dB can be observed, ranging from 1541 nm to 1550 nm. The ER_{TM} is originated from the weakly reflected TM_0 mode.
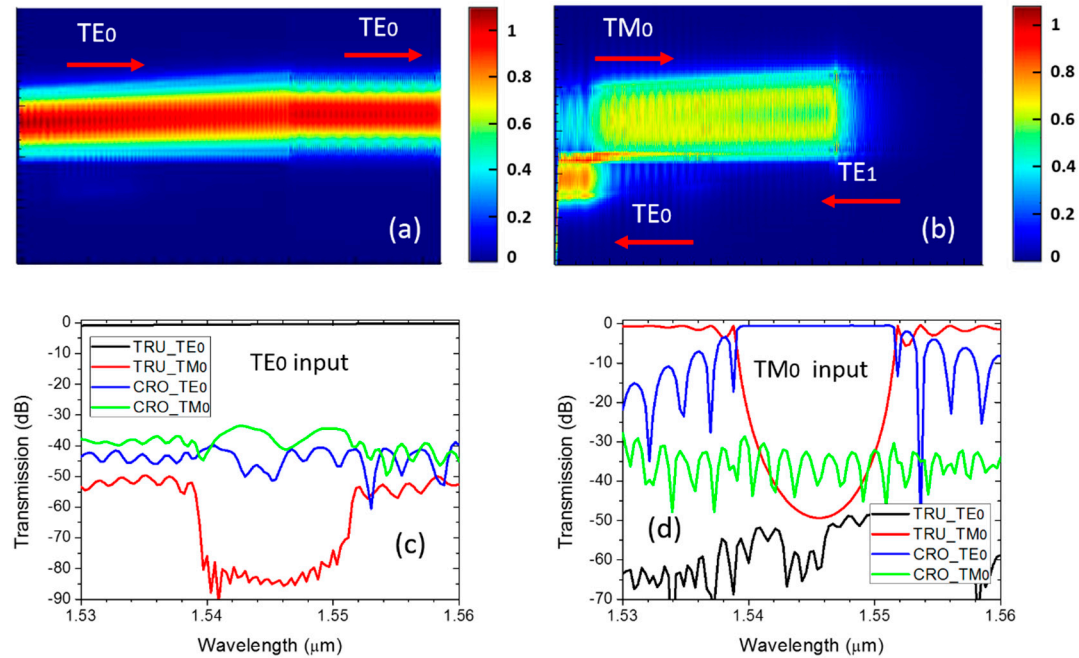

Figure 9. The light propagation profiles (electric field intensity |E|) for the PSR when (**a**) TE_0 mode and (**b**) TM_0 mode are launched at wavelength of 1.546 µm. The simulated transmission spectra of the proposed PSR when (**c**) TE_0 mode and (**d**) TM_0 mode are launched.

We further investigate the fabrication tolerance of the proposed PSR, assuming there is a width variation of W_2 and corrugation δw. As shown in Figure 10a, when TM_0 mode is launched, the PSR exhibits a performance of < 0.5 dB IL and > 30 dB CT, when ΔW_2 changes from −10 nm to 10 nm. The reason can be explained by the fact that the effective refractive index in MWG is sensitive to the width variation; therefore, the phase-match condition and stopband are affected. However, the transmission of TE_0 mode (Figure 10b) is only slightly affected by ΔW_2; the CT is > 36 dB, and IL is < 0.6 dB, showing a robust performance. The device performance affected by the corrugation width δw is shown in Figure 10c,d. For the TM_0 mode, a high CT of > 20 dB is obtained, when Δδw varies from −7.5 nm to 7.5 nm, assuming W_2 = 0.9 µm. However, this influence is slight for TE_0 mode (Figure 10d). Overall, the proposed PSR exhibits different performance according to the structure variations, for TE_0 mode and TM_0 mode, respectively. Additionally, for the injected TM_0 mode, the influence of Δδw is more significant than ΔW_2. The proposed device can be fabricated by advanced fabrication technologies.
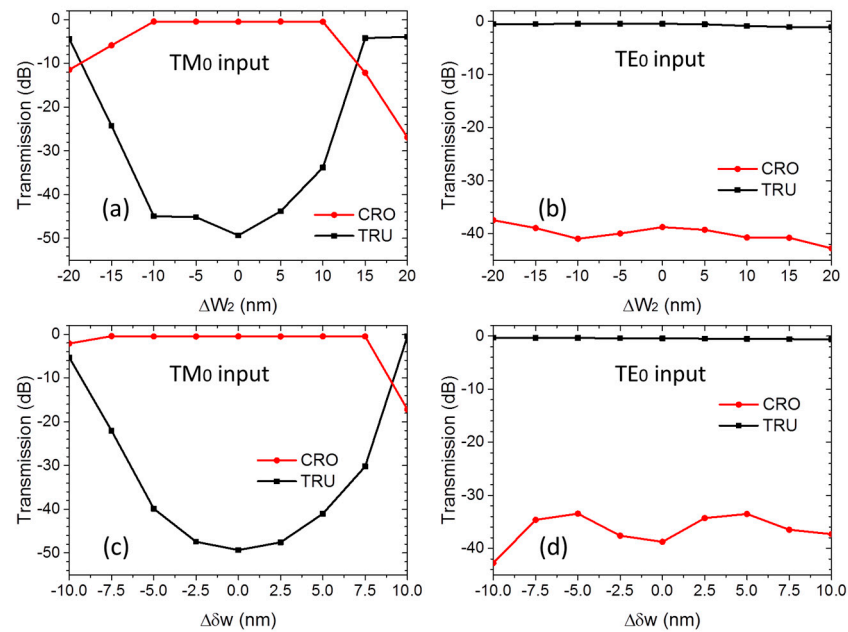
Figure 10. Dependence of transmission on (**a**,**b**) width deviation ΔW_2 and (**c**,**d**) corrugation width deviation $\Delta \delta w$ for TE_0 and TM_0 incidence at wavelength of 1.546 μm.

4. Fabrication and Measurement

We fabricated the proposed PSR on the SOI platform with a 220 nm thick silicon layer and a 2 μm thick oxide layer. The silicon waveguides were first patterned via electron beam lithography (EBL), then etched by the inductively coupled plasma (ICP) etching process. The focused TM grating couplers (pitch = 1.19 μm, duty cycle = 0.5) and linearly tapered TE grating couplers (pitch = 0.662 μm, duty cycle = 0.5) were adopted for fiber-chip coupling and polarization selectivity, with the same coupling angle of 20°. To make a full characterization for different polarization conversion scenarios, four sets of PSRs with TE/TM grating couplers at the input/output ports were fabricated, as shown in Figure 11a. It should be noted that the length of AC was chosen as 350 μm for complete mode conversion [4]. Figure 11b,c show the scanning electric microscopy (SEM) image of the taper and uniform grating section. We can see that the taper section and the designed corrugations on MWG have been accurately fabricated.
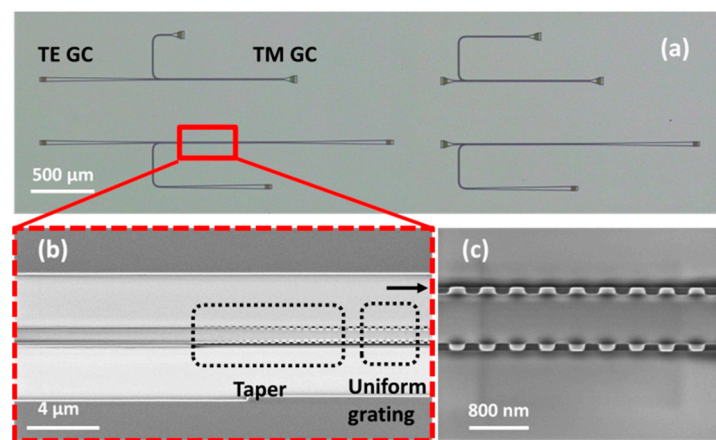

Figure 11. (**a**) The microscope image for the fabricated PSR. The scanning electric microscopy (SEM) image for (**b**) linearly taper section and (**c**) zoom-in of uniform grating section.

To experimentally characterize the fabricated devices, light was first generated from a C-band tunable laser, with its polarization state controlled by a polarization controller.

The position and angle of the two coupling fibers were aligned utilizing two six-axis stages. The laser source and power meter were connected by a computer to implement wavelength sweeping and power data recording. Figure 12a,b show the measured transmission spectra of the fabricated PSR when TE_0 mode and TM_0 mode are launched, which are normalized with respect to the transmission of grating couplers on the same chip. As depicted in Figure 12a, the TE_0 mode propagates to the TRU port with average IL_{TE} of 1.2 dB. The ER_{TE} is > 53 dB and CT_{TE} is < −26.4 dB, around the central wavelength of 1555 nm. As shown in Figure 12b, when the TM_0 mode is launched, light outputs from the CRO port; the average IL_{TM} is 1.5 dB, ER_{TM} of > 31 dB, and CT_{TM} of > −30 dB can be observed ranging from 1552 nm to 1562 nm. We can also observe about 10 nm central wavelength shifting, compared with the simulation results, which comes from the fabrication errors such as the variation of waveguide width, corrugation width, or waveguide thickness.
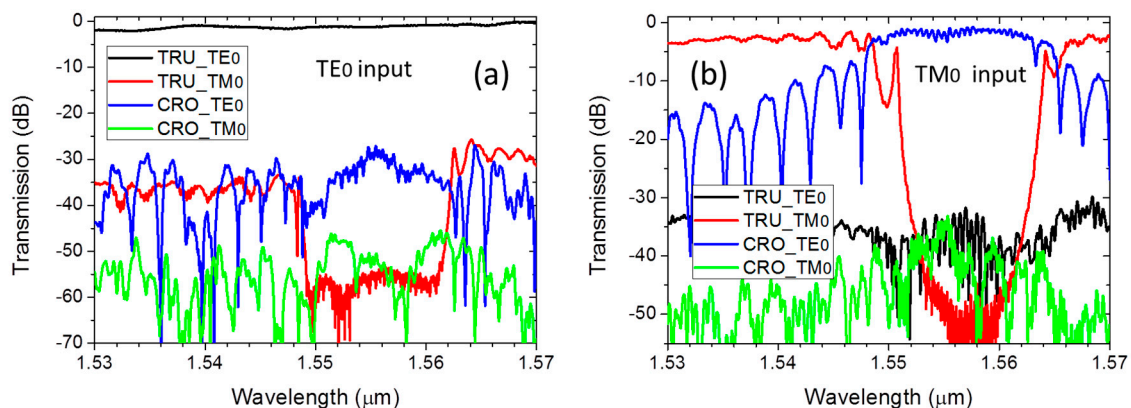
Figure 12. (**a**) Measured transmission spectra of the fabricated PSRs at through port and (**b**) cross port when TE_0 and TM_0 mode are launched.

5. Conclusions

In summary, we have presented a novel PSR based on MWG, on the SOI platform. Bloch mode hybridization in MSB is exploited to achieve a high polarization conversion efficiency. The fabricated devices exhibit a high extinction ratio of > 53 dB and > 31 dB, low crosstalk of < −26.4 dB and < −40 dB for the injected TE_0 and TM_0 mode around the central wavelength. We believe that the proposed PSR could be applied in integrated polarization diversity circuits, especially for applications requiring spectra manipulation such as polarization insensitive wavelength division (de)multiplexer and multichannel polarization-multiplexed differential quadrature phase-shift keying (PM-DQPSK) transceiver. Additionally, the polarization conversion approach provides opportunities to develop novel polarization management devices.

Author Contributions: Conceptualization, Y.L. (Yannong Luo) and X.C.; methodology, Y.L. (Yannong Luo), R.G. and H.L.; software, Y.L. (Yannong Luo) and R.G.; validation, Y.L. (Yannong Luo), L.Z. and M.A.; formal analysis, Y.L. (Yannong Luo), R.G. and W.L.; investigation, Y.L. (Yannong Luo) and J.Y.; resources, J.X.; data curation, Y.L. (Yannong Luo); writing—original draft preparation, Y.L. (Yannong Luo); writing—review and editing, Y.L. (Yannong Luo), M.W. and Q.L.; visualization, X.C.; supervision, Y.L. (Yongqing Li) and X.C.; project administration, Y.L. (Yannong Luo); funding acquisition, Y.L. (Yannong Luo) and X.C. All authors have read and agreed to the published version of the manuscript.

References

1. Dai, D.; Bowers, J.E. Novel concept for ultracompact polarization splitter-rotator based on silicon nanowires. *Opt. Exp.* **2011**, *19*, 10940–10949. [CrossRef]
2. Dai, D.; Liu, L.; Gao, S.; Xu, D.X.; He, S. Polarization management for silicon photonic integrated circuits. *Laser Photonics Rev.* **2013**, *7*, 303–328. [CrossRef]
3. Doerr, C.; Chen, L.; Vermeulen, D.; Nielsen, T.; Azemati, S.; Stulz, S.; McBrien, G.; Xu, X.-M.; Mikkelsen, B.; Givehchi, M. Single-chip silicon photonics 100-Gb/s coherent transceiver. In Proceedings of the Optical Fiber Communication Conference, San Francisco, CA, USA, 9–13 March 2014; p. Th5C.1.
4. Sacher, W.D.; Barwicz, T.; Taylor, B.J.F.; Poon, J.K.S. Polarization rotator-splitters in standard active silicon photonics platforms. *Opt. Exp.* **2014**, *22*, 3777–3786. [CrossRef]
5. Wang, Y.; Ma, M.; Yun, H.; Lu, Z.; Wang, X.; Jaeger, N.A.; Chrostowski, L. Ultra-compact sub-wavelength grating polarization splitter-rotator for silicon-on-insulator platform. *IEEE Photon. J.* **2016**, *8*, 1–9. [CrossRef]
6. Keyvaninia, S.; Boerma, H.; Wössner, M.; Ganzer, F.; Runge, P.; Schell, M. Highly efficient passive InP polarization rotator-splitter. *Opt. Exp.* **2019**, *27*, 25872–25881. [CrossRef] [PubMed]
7. Chung, C.-J.; Midkiff, J.; Yoo, K.M.; Rostamian, A.; Guo, J.; Chen, R.T.; Chakravarty, S. InP-based polarization rotator-splitter for mid-infrared photonic integration circuits. *AIP Adv.* **2019**, *9*, 015303. [CrossRef]
8. Dai, X.; Lu, Q.; Guo, W. Fabrication-Tolerant Polarization Rotator-Splitter based on Silicon Nitride Platform. In Proceedings of the Optical Fiber Communication Conference, Washington, DC, USA, 6–11 June 2021; p. Th1A.31.
9. Chen, Z.; Pan, Y.; Liu, X.; Lin, H.; Zhong, X.; Cai, X. Single-step Etching Polarization Splitter-rotator based on Lithium Niobate Ridge Waveguide. In Proceedings of the Asia Communications and Photonics Conference, Chengdu, China, 2–5 November 2019; p. M4A.285.
10. Zhang, L.; Yang, S.; Zhang, G.; Fu, X.; Yang, L. Broadband 2 × 2 Polarization Splitter-Rotator Based on an Adiabatic Asymmetric Directional Coupler on the Lithium-Niobate-on-Insulator. In Proceedings of the Asia Communications and Photonics Conference, Beijing, China, 24–27 October 2020; p. M4A.176.
11. Tu, X.; Li, M.; Xing, J.; Fu, H.; Geng, D. Compact PSR based on an asymmetric bi-level lateral taper in an adiabatic directional coupler. *J. Light. Technol.* **2016**, *34*, 985–991. [CrossRef]
12. Wang, J.; Qi, M.; Xuan, Y.; Huang, H.; Li, Y.; Li, M.; Chen, X.; Jia, Q.; Sheng, Z.; Wu, A. Proposal for fabrication-tolerant SOI polarization splitter-rotator based on cascaded MMI couplers and an assisted bi-level taper. *Opt. Exp.* **2014**, *22*, 27869–27879. [CrossRef] [PubMed]
13. Bai, B.; Liu, L.; Zhou, Z. Ultracompact, high extinction ratio polarization beam splitter-rotator based on hybrid plasmonic-dielectric directional coupling. *Opt. Lett.* **2017**, *42*, 4752–4755. [CrossRef] [PubMed]
14. Chen, L.; Doerr, C.R.; Chen, Y.-K. Compact polarization rotator on silicon for polarization-diversified circuits. *Opt. Lett.* **2011**, *36*, 469–471. [CrossRef]
15. Guan, H.; Novack, A.; Streshinsky, M.; Shi, R.; Fang, Q.; Lim, A.E.-J.; Lo, G.-Q.; Baehr-Jones, T.; Hochberg, M. CMOS-compatible highly efficient polarization splitter and rotator based on a double-etched directional coupler. *Opt. Exp.* **2014**, *22*, 2489–2496. [CrossRef] [PubMed]
16. Dai, D.; Wu, H. Realization of a compact polarization splitter-rotator on silicon. *Opt. Lett.* **2016**, *41*, 2346–2349. [CrossRef] [PubMed]
17. Yin, Y.; Li, Z.; Dai, D. Ultra-broadband polarization splitter-rotator based on the mode evolution in a dual-core adiabatic taper. *J. Light. Technol.* **2017**, *35*, 2227–2233. [CrossRef]
18. Liu, L.; Ding, Y.; Yvind, K.; Hvam, J.M. Silicon-on-insulator polarization splitting and rotating device for polarization diversity circuits. *Opt. Exp.* **2011**, *19*, 12646–12651. [CrossRef]
19. Ding, Y.; Liu, L.; Peucheret, C.; Ou, H. Fabrication tolerant polarization splitter and rotator based on a tapered directional coupler. *Opt. Exp.* **2012**, *20*, 20021–20027. [CrossRef]
20. Tan, K.; Huang, Y.; Lo, G.-Q.; Lee, C.; Yu, C. Compact highly-efficient polarization splitter and rotator based on 90° bends. *Opt. Exp.* **2016**, *24*, 14506–14512. [CrossRef]
21. Zafar, H.; Pereira, M.F.; Kennedy, K.L.; Anjum, D.H. Fabrication-tolerant and CMOS-compatible polarization splitter and rotator based on a compact bent-tapered directional coupler. *AIP Adv.* **2020**, *10*, 125214. [CrossRef]
22. Xu, H.; Shi, Y. Ultra-broadband silicon polarization splitter-rotator based on the multi-mode waveguide. *Opt. Exp.* **2017**, *25*, 18485–18491. [CrossRef]
23. Jeong, S.-H.; Onawa, Y.; Shimura, D.; Okayama, H.; Aoki, T.; Yaegashi, H.; Horikawa, T.; Nakamura, T. Polarization diversified 16λ demultiplexer based on silicon wire delayed interferometers and arrayed waveguide gratings. *J. Light. Technol.* **2020**, *38*, 2680–2687. [CrossRef]
24. Onawa, Y.; Okayama, H.; Shimura, D.; Takahashi, H.; Yaegashi, H.; Sasaki, H. Polarisation insensitive wavelength de-multiplexer using arrayed waveguide grating and polarisation rotator/splitter. *Electron. Lett.* **2019**, *55*, 475–476. [CrossRef]

25. Chen, S.; Fu, X.; Wang, J.; Shi, Y.; He, S.; Dai, D. Compact dense wavelength-division (de) multiplexer utilizing a bidirectional arrayed-waveguide grating integrated with a Mach–Zehnder interferometer. *J. Light. Technol.* **2015**, *33*, 2279–2285. [CrossRef]

26. Olivier, S.; Rattier, M.; Benisty, H.; Weisbuch, C.; Smith, C.; De La Rue, R.; Krauss, T.; Oesterle, U.; Houdré, R. Mini-stopbands of a one-dimensional system: The channel waveguide in a two-dimensional photonic crystal. *Phys. Rev. B* **2001**, *63*, 113311. [CrossRef]

27. Olivier, S.; Benisty, H.; Weisbuch, C.; Smith, C.J.; Krauss, T.F.; Houdré, R. Coupled-mode theory and propagation losses in photonic crystal waveguides. *Opt. Exp.* **2003**, *11*, 1490–1496. [CrossRef]

28. Cao, T.; Cryan, M.J.; Ivanov, P.S.; Ho, D.; Ren, B.; Craddock, I.J.; Rorison, J.M.; Railton, C.J. Modeling of chirped pulse propagation through a mini-stop band in a two-dimensional photonic crystal waveguide. *J. Opt. Soc. Am. B* **2007**, *24*, 1575–1583. [CrossRef]

29. Benisty, H.; Cambournac, C.; Van Laere, F.; Van Thourhout, D. Photonic-crystal demultiplexer with improved crosstalk by second-order cavity filtering. *J. Light. Technol.* **2010**, *28*, 1201–1208. [CrossRef]

30. Shahid, N.; Amin, M.; Naureen, S.; Swillo, M.; Anand, S. Junction-type photonic crystal waveguides for notch-and pass-band filtering. *Opt. Exp.* **2011**, *19*, 21074–21080. [CrossRef] [PubMed]

31. Ayre, M.; Cambournac, C.; Khayam, O.; Benisty, H.; Stomeo, T.; Krauss, T. Photonic crystal waveguides for coarse-selectivity devices. *Photonics Nanostruct.* **2008**, *6*, 19–25. [CrossRef]

32. Moore, S.; O'Faolain, L.; White, T.; Krauss, T. Photonic crystal laser with mode selective mirrors. *Opt. Exp.* **2008**, *16*, 1365–1370. [CrossRef]

33. Qiu, H.; Jiang, J.; Yu, P.; Yang, J.; Yu, H.; Jiang, X. Broad bandwidth and large fabrication tolerance polarization beam splitter based on multimode anti-symmetric Bragg sidewall gratings. *Opt. Lett.* **2017**, *42*, 3912–3915. [CrossRef]

34. Huang, Q.; Jie, K.; Liu, Q.; Huang, Y.; Wang, Y.; Xia, J. Ultra-compact, broadband tunable optical bandstop filters based on a multimode one-dimensional photonic crystal waveguide. *Opt. Exp.* **2016**, *24*, 20542–20553. [CrossRef]

35. Shi, W.; Yun, H.; Lin, C.; Greenberg, M.; Wang, X.; Wang, Y.; Fard, S.T.; Flueckiger, J.; Jaeger, N.A.; Chrostowski, L. Ultra-compact, flat-top demultiplexer using anti-reflection contra-directional couplers for CWDM networks on silicon. *Opt. Exp.* **2013**, *21*, 6733–6738. [CrossRef] [PubMed]

36. Chen, J.; Shi, Y. Flat-Top CWDM (De) multiplexers Based on Contra-directional Couplers with Subwavelength Gratings. *IEEE Photon. Technol. Lett.* **2019**, *31*, 2003–2006. [CrossRef]

37. Chen, L.; Doerr, C.R.; Chen, Y.-k. Polarization-diversified DWDM receiver on silicon free of polarization-dependent wavelength shift. In Proceedings of the Optical Fiber Communication Conference, Los Angeles, CA, USA, 4–8 March 2012; pp. 1–3.

38. Corzine, S.W.; Evans, P.; Fisher, M.; Gheorma, J.; Kato, M.; Dominic, V.; Samra, P.; Nilsson, A.; Rahn, J.; Lyubomirsky, I. Large-scale InP transmitter PICs for PM-DQPSK fiber transmission systems. *IEEE Photon. Technol. Lett.* **2010**, *22*, 1015–1017. [CrossRef]

39. Wang, X.; Wang, Y.; Flueckiger, J.; Bojko, R.; Liu, A.; Reid, A.; Pond, J.; Jaeger, N.A.; Chrostowski, L. Precise control of the coupling coefficient through destructive interference in silicon waveguide Bragg gratings. *Opt. Lett.* **2014**, *39*, 5519–5522. [CrossRef]

40. Jiang, J.; Qiu, H.; Wang, G.; Li, Y.; Dai, T.; Mu, D.; Yu, H.; Yang, J.; Jiang, X. Silicon lateral-apodized add–drop filter for on-chip optical interconnection. *Appl. Opt.* **2017**, *56*, 8425–8429. [CrossRef] [PubMed]

41. Cheng, R.; Chrostowski, L. Spectral Design of Silicon Integrated Bragg Gratings: A Tutorial. *J. Light. Technol.* **2020**, *39*, 712–729. [CrossRef]

42. Liu, Y.; Wang, S.; Wang, Y.; Liu, W.; Xie, H.; Yao, Y.; Song, Q.; Zhang, X.; Yu, Y.; Xu, K. Subwavelength polarization splitter–rotator with ultra-compact footprint. *Opt. Lett.* **2019**, *44*, 4495–4498. [CrossRef]